Here There Be (Dusty) Monsters: High-redshift Active Galactic Nuclei Are Dustier than Their Hosts

Madisyn Brooks, Raymond Simons, Jonathan Trump, Anthony Taylor, Micaela Bagley, Bren Backhaus, Kelcey Davis, Véronique Buat, Nikko Cleri, Alexander de la Vega, et al.

The Astrophysical Journal, 986:177 (10pp), 2025 June 20 https://doi.org/10.3847/1538-4357/addac4

Here There Be (Dusty) Monsters: High-redshift Active Galactic Nuclei Are Dustier than Their Hosts

Madisyn Brooks[1], Raymond C. Simons[1,2], Jonathan R. Trump[1], Anthony J. Taylor[3], Micaela B. Bagley[3,4], Bren Backhaus[5], Kelcey Davis[1], Véronique Buat[6,7], Nikko J. Cleri[8,9,10], Alexander de la Vega[11], Steven L. Finkelstein[3,12], Michaela Hirschmann[13], Benne W. Holwerda[14], Dale D. Kocevski[15], Anton M. Koekemoer[16], Ray A. Lucas[16], Fabio Pacucci[17,18], and Lise-Marie Seillé[6]
[1] Department of Physics, 196A Auditorium Road, Unit 3046, University of Connecticut, Storrs, CT 06269, USA
[2] Department of Engineering and Physics, Providence College, 1 Cunningham Square, Providence, RI 02918, USA
[3] Department of Astronomy, The University of Texas at Austin, Austin, TX, USA
[4] Astrophysics Science Division, NASA Goddard Space Flight Center, 8800 Greenbelt Road, Greenbelt, MD 20771, USA
[5] Department of Physics and Astronomy, University of Kansas, Lawrence, KS 66045, USA
[6] Aix Marseille Univ, CNRS, CNES, LAM, Marseille, France
[7] Institut Universitaire de France (IUF), Paris, France
[8] Department of Astronomy and Astrophysics, The Pennsylvania State University, University Park, PA 16802, USA
[9] Institute for Computational and Data Sciences, The Pennsylvania State University, University Park, PA 16802, USA
[10] Institute for Gravitation and the Cosmos, The Pennsylvania State University, University Park, PA 16802, USA
[11] Department of Physics and Astronomy, University of California, 900 University Avenue, Riverside, CA 92521, USA
[12] Cosmic Frontier Center, The University of Texas at Austin, Austin, TX, USA
[13] Institute of Physics, Laboratory of Galaxy Evolution, Ecole Polytechnique Fédérale de Lausanne (EPFL), Observatoire de Sauverny, 1290 Versoix, Switzerland
[14] Department of Physics, University of Louisville, Natural Science Building 102, Louisville, KY 40292, USA
[15] Department of Physics and Astronomy, Colby College, Waterville, ME 04901, USA
[16] Space Telescope Science Institute, 3700 San Martin Drive, Baltimore, MD 21218, USA
[17] Center for Astrophysics | Harvard & Smithsonian, 60 Garden Street, Cambridge, MA 02138, USA
[18] Black Hole Initiative, Harvard University, 20 Garden Street, Cambridge, MA 02138, USA
Received 2024 October 9; revised 2025 April 21; accepted 2025 April 29; published 2025 June 17

Abstract

JWST spectroscopy has discovered a population of $z \gtrsim 3.5$ galaxies with broad Balmer emission lines and narrow forbidden lines that are consistent with hosting active galactic nuclei (AGN). Many of these systems, now known as "little red dots," are compact and have unique colors that are very red in the optical/near-infrared and blue in the ultraviolet. The relative contribution of galaxy starlight and AGN to these systems remains uncertain, especially for the galaxies with unusual blue+red spectral energy distributions. In this work, we use Balmer decrements to measure the independent dust attenuation of the broad and narrow emission-line components of a sample of 29 broad-line AGN identified from three public JWST spectroscopy surveys: CEERS, JADES, and RUBIES. Stacking the narrow components from the spectra of 25 sources with broad Hα and no broad Hβ results in a median narrow Hα/H$\beta = 2.47^{+0.05}_{-0.05}$ (consistent with $A_v = 0$) and broad Hα/Hβ >8.85 ($A_v > 3.63$). The narrow and broad Balmer decrements imply little to no attenuation of the narrow emission lines, which are consistent with being powered by star formation and located on larger physical scales. Meanwhile, the lower limit in the broad Hα/Hβ decrement, with broad Hβ undetected in the stacked spectrum of 25 broad Hα AGN, implies significant dust attenuation of the broad-line emitting region that is presumably associated with the central AGN. Our results indicate that these systems, on average, are consistent with heavily dust-attenuated AGN powering the red parts of their SED, while their blue UV emission is powered by unattenuated star formation in the host galaxy.

Unified Astronomy Thesaurus concepts: Active galactic nuclei (16); AGN host galaxies (2017); High-redshift galaxies (734); Supermassive black holes (1663); Spectroscopy (1558)

Materials only available in the online version of record: figure set, machine-readable tables

1. Introduction

JWST observations of extragalactic deep fields have unveiled a new regime of black hole (BH) science; faint, high-redshift ($z \gtrsim 3.5$) active galactic nuclei (AGN) are being detected in abundance through broad Balmer line emission and are consistent with being powered by BHs with inferred masses 10^6–10^8 $M_\odot$ (Y. Harikane et al. 2023a; M. Killi et al. 2024; D. D. Kocevski et al. 2023; V. Kokorev et al. 2023; R. L. Larson et al. 2023; R. Maiolino et al. 2024; H. Übler et al. 2023; J. E. Greene et al. 2024; D. D. Kocevski et al. 2024; A. J. Taylor et al. 2024). This sample of AGN allows us to probe the low-mass distribution of BHs at high redshifts, providing insight into the first black holes, i.e., the population of BH seeds (e.g., V. Bromm & A. Loeb 2003; M. Volonteri et al. 2003; G. Lodato & P. Natarajan 2006; K. Inayoshi et al. 2020; F. Pacucci et al. 2023).

A fraction (∼20%) of broad-line (BL) identified AGN are compact sources that appear heavily obscured and are characterized by a "V-shaped" spectral energy distribution (SED) with a steep red continuum in the rest-frame optical and elevated blue colors in the UV (G. Barro et al. 2024; J. E. Greene et al. 2024; D. D. Kocevski et al. 2024; J. Matthee et al. 2024). The emission mechanisms that power the red

+blue colors in these sources, now colloquially known as "little red dots" (LRDs; J. Matthee et al. 2024), have been heavily debated in the literature. The excess of UV light can be explained by light scattered from a central AGN or from an unobscured host galaxy, while the optical colors could be a dust-reddened AGN or emission from starburst galaxies (D. D. Kocevski et al. 2023; I. Labbe et al. 2025; H. B. Akins et al. 2024; G. Barro et al. 2024; Z. Li et al. 2025). JWST-detected BL AGN are more abundant (Y. Harikane et al. 2023a, 2023b; V. Kokorev et al. 2023; J. E. Greene et al. 2024), about 1–2 dex higher in number density than what is expected from local quasar studies (M. Vestergaard & P. S. Osmer 2009; B. C. Kelly & Y. Shen 2013; Y. Matsuoka et al. 2018) and provide a unique population to further explore the $M_{\rm BH}$–M_* relation in the early Universe (F. Pacucci et al. 2023; E. Durodola et al. 2025).

Notably, X-ray emission studies of LRDs have reported nondetections (T. T. Ananna et al. 2024; J. Lyu et al. 2024; J. Matthee et al. 2024), and even stacking techniques still fail to produce an X-ray detection (R. Maiolino et al. 2025) or suggest that LRDs are an intrinsically X-ray weak population (M. Yue et al. 2024). The failure to detect BL AGN and/or LRDs in X-ray observations could be explained by X-ray absorption by gas in the BL region with large covering factors (R. Maiolino et al. 2025) and/or super-Eddington accretion onto slowly spinning BHs, a combination that leads to intrinsically weak SEDs in the X-rays (I. Juodžbalis et al. 2024; E. Lambrides et al. 2024; F. Pacucci & R. Narayan 2024). Analyses of two X-ray-confirmed AGN, at $z = 3.1$ and $z = 4.66$ in B. Wang et al. (2025) and D. D. Kocevski et al. (2024), find that their X-ray emission is consistent with a dust-reddened AGN and that they could be lower-redshift analogs of the LRD population.

In this paper, we investigate the optical dust attenuation of high-redshift ($z > 3.5$) BL AGN identified in the JWST deep fields. Our sample consists of 29 spectroscopically confirmed BL AGN detected through broad Hα emission and is gathered from three large public spectroscopy surveys: Cosmic Evolution Early Release Science Survey (CEERS), JWST Advanced Deep Extragalactic Survey (JADES), and RUBIES. We derive narrow line (NL) and BL Balmer decrements, using Hα and Hβ, for this sample of BL AGN to explore different physical scenarios that can contribute to the "V-shaped" SEDs associated with LRDs. We stack sources that show no broad Hβ emission (25/29) to further constrain the dust attenuation seen in the narrow and BL emission.

This paper is presented as follows. In Section 2, we describe our AGN sample; in Section 3, we describe our line-fitting technique and Balmer decrement measurements; and in Section 4, we describe our results and their implications for BL AGN. For this work, we assume a flat ΛCDM cosmology with $H_0 = 67.4\,{\rm km\,s^{-1}\,Mpc^{-1}}$ and $\Omega_M = 0.315$ (Planck Collaboration et al. 2020).

2. Observational Data Set

We select AGN in the JWST deep fields that exhibit broad Hα emission and have both Hα and Hβ spectral coverage (Y. Harikane et al. 2023a; D. D. Kocevski et al. 2023; R. Maiolino et al. 2024; A. J. Taylor et al. 2024). We analyzed data from CEERS (S. L. Finkelstein et al. (2023), JADES (F. D'Eugenio et al. 2025), and RUBIES (A. de Graaff et al. 2025). Our sample consists of galaxies observed with NIRSpec medium resolution ($\lambda/\Delta\lambda \sim 1000$) spectra. For this study, we do not use PRISM spectra; PRISM spectra have strongly varying wavelength-dependent spectral resolutions that can make it challenging to resolve emission (broad+narrow) on the bluer end of the spectrum, like Hβ. The complete sample studied in this paper spans the redshift range of $3.87 < z < 6.76$. This redshift range is chosen to ensure coverage of both Hα and Hβ in the medium-grating observations. In total, the sample contains 29 sources: 5 observed through CEERS, 10 through JADES, and 14 through RUBIES. A brief description of the observation programs used in this study follows, and our sample selection is described in Section 2.4. Our complete sample of BL AGN is shown in Table 1, and the distribution of Hα luminosities is shown in Figure 1.

2.1. CEERS

CEERS covered ∼100 arcmin^2 of the Extended Groth Strip (EGS; S. Finkelstein et al. 2023). Six NIRSpec pointings were observed with the G140M/F100LP, G235M/F170LP, and G395M/F290LP grating/filter pairs, resulting in a complete wavelength coverage from ∼1 to 5 μm. Each NIRSpec pointing was observed for 0.86 hr in each grating. For this study, we use only the G235M/170LP and G395M/F290LP grating/filter pairs. These two configurations have coverage of both Hα and Hβ over a redshift range of $2.41 < z < 6.77$. The spectroscopic data were processed with the STScI JWST Calibration Pipeline v1.8.5. We refer to P. Arrabal Haro et al. (2023) for a full description of the NIRSpec data reduction for CEERS.

2.2. JADES

The JWST Advanced Deep Extragalactic Survey (JADES) covered ∼175 arcmin^2 in the GOODS-S and GOODS-N fields (M. Rieke et al. 2023). We use NIRSpec data publicly released as part of JADES DR3 (F. D'Eugenio et al. 2025) and focus only on the G235M/170LP and G395M/F290LP grating/filter pairs. The JADES spectroscopic data were processed with a custom pipeline described in P. Ferruit et al. (2022). JADES observations were split into three visits, with individual objects being observed with one, two, or three visits at 2.3 hr exposure time per visit. Objects observed in each visit reached up to ∼7 hr of exposure time. We use the strong emission line flux catalogs included in the JADES DR3 to plot Hα luminosities in Figure 1. We refer to D. J. Eisenstein et al. (2023), A. J. Bunker et al. (2024), and F. D'Eugenio et al. (2025) for a full description of the JADES survey and NIRSpec data reduction.

2.3. RUBIES

RUBIES observed six pointings in the CEERS (EGS) field and six pointings in the PRIMER-UDS (Ultra Deep South) Field (A. de Graaff et al. 2025). The spectroscopic data were processed with the STScI JWST Calibration Pipeline version 1.13.4. RUBIES observed with the G395M/F290LP grating/filter pair, giving us our highest-redshift sources. Sources observed only with the G395M grating that cover both the Hα and Hβ wavelength range will fall within redshifts $4.90 < z < 6.77$. Each pointing in this survey had an exposure time of 0.80 hr. We refer to A. J. Taylor et al. (2024) for a full description of the RUBIES NIRSpec data reduction used here.

Table 1
BL AGN Sample

Name	R.A. (deg)	Decl. (deg)	z_{spec}	β_{opt}	β_{UV}
CEERS-11728	215.084870	52.970738	3.869	0.46 ± 0.23	…[a]
JADES-GN-73488	189.197396	62.177233	4.133	−2.38 ± 2.00	−1.96 ± 0.11
JADES-GN-11836	189.220587	62.263675	4.409	−2.12 ± 0.37	−1.87 ± 0.05
JADES-GN-53757	189.269778	62.194208	4.448	−1.33 ± 0.16	…[a]
CEERS-1665	215.178197	53.059349	4.483	−0.49 ± 1.18	−0.87 ± 0.27
CEERS-1236	215.145291	52.967291	4.484	0.99 ± 0.06	−1.81 ± 0.01
JADES-GS-8083	53.132846	−27.801860	4.648	−0.55 ± 0.97	…[a]
RUBIES-EGS-46985	214.805654	52.809497	4.963	−2.03 ± 0.81	−2.23 ± 0.04
RUBIES-EGS-17416	214.949482	52.845415	5.000	1.92 ± 0.12	−1.98 ± 0.34
JADES-GN-62309	189.248977	62.218350	5.172	0.34 ± 1.19	−2.23 ± 0.21
RUBIES-EGS-17301	214.987485	52.873115	5.226	1.99 ± 0.80	−1.33 ± 0.07
JADES-GN-77652	189.293228	62.199003	5.229	0.09 ± 1.65	−1.69 ± 0.20
RUBIES-EGS-50052[b]	214.823454	52.830277	5.240	−1.76 ± 1.03	−2.11 ± 0.05
RUBIES-EGS-13872	215.132933	52.970705	5.262	1.34 ± 0.56	−2.30 ± 0.15
RUBIES-EGS-42046	214.795368	52.788847	5.279	0.46 ± 0.57	−1.99 ± 0.06
RUBIES-EGS-60935	214.923373	52.925593	5.287	−0.09 ± 1.20	−0.82 ± 1.04
RUBIES-EGS-926125	215.137081	52.988554	5.284	0.95 ± 1.07	−1.31 ± 0.07
CEERS-746	214.809145	52.868483	5.624	−0.59 ± 1.13	−2.51 ± 0.13
JADES-GN-1093	189.179742	62.224628	5.595	−0.45 ± 1.26	−1.46 ± 0.01
RUBIES-UDS-29813	34.453355	−5.270717	5.440	−1.45 ± 0.11	1.73 ± 0.75
RUBIES-UDS-19521	34.383672	−5.287732	5.669	0.64 ± 0.04	−1.64 ± 0.27
RUBIES-UDS-47509	34.264602	−5.232586	5.673	0.31 ± 0.08	−1.99 ± 0.13
RUBIES-EGS-27915	214.844229	52.789595	5.680	0.80 ± 0.31	−2.28 ± 0.03
JADES-GN-61888	189.168016	62.217013	5.875	−5.56 ± 1.85	−2.15 ± 0.03
JADES-GS-10013704	53.126535	−27.818092	5.919	0.49 ± 0.27	−1.64 ± 0.12
CEERS-397	214.836183	52.882678	6.000	0.09 ± 0.52	−2.24 ± 0.10
RUBIES-EGS-49140	214.892248	52.877410	6.685	1.82 ± 0.97	−0.67 ± 0.04
JADES-GN-954	189.151966	62.259635	6.760	−1.22 ± 0.55	−1.79 ± 0.00
RUBIES-UDS-807469	34.376139	−5.310366	6.778	−0.37 ± 0.87	−1.79 ± 0.03

Note.
[a] Denotes β measurements that we were unable to constrain due to poor photometry.
[b] RUBIES-EGS-50052 is the same source as CEERS-02782 reported in Y. Harikane et al. (2023a). We elected to use RUBIES-EGS-50052 in this paper due to its higher SNR as noted by A. J. Taylor et al. (2024).

(This table is available in machine-readable form in the online article.)

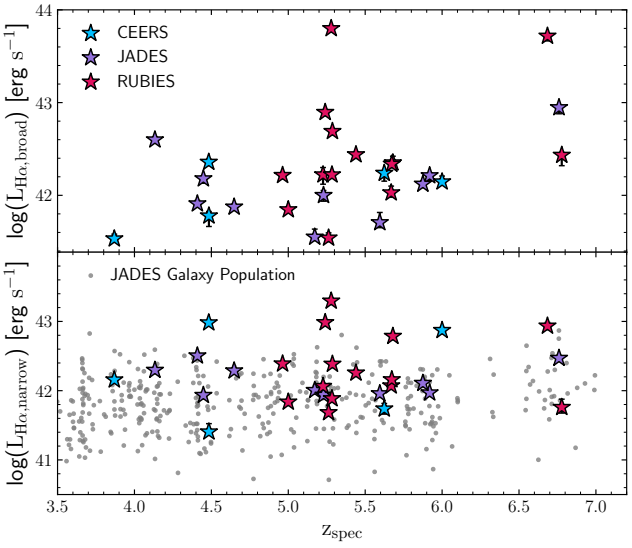

Figure 1. BL component Hα luminosity (top) and NL component Hα luminosity (bottom) as a function of redshift for our sample of 29 BL AGN, spanning $4.13 < z < 6.78$. CEERS sources are shown in blue, JADES sources are shown in purple, and RUBIES are shown in red. The full narrow Hα luminosity distribution for the JADES spectroscopic population is shown by the small gray circles.

The specific RUBIES observations analyzed in this paper can be accessed via MAST: doi:10.17909/9d12-3f91.

2.4. BL AGN Sample

Our sample consists of AGN identified from broad Hα emission and is collected from Y. Harikane et al. (2023b), D. D. Kocevski et al. (2023), R. Maiolino et al. (2024), and A. J. Taylor et al. (2024). We note that the full BL AGN sample in the respective papers might not be represented in this sample. We select sources with significantly detected ($>3\sigma$) broad Hα emission and sufficient ($\pm 0.05\ \mu$m) spectral coverage around the Hβ emission line. We now briefly describe the detection method used by each study, but we refer to the respective papers for a full description.

2.4.1. CEERS BL AGN

The sources in CEERS are described in detail in D. D. Kocevski et al. (2023), Y. Harikane et al. (2023a), and A. J. Taylor et al. (2024). The two BL AGN identified in D. D. Kocevski et al. (2023) are also identified in Y. Harikane et al. (2023a). Y. Harikane et al. (2023a) select sources that have a broad (FWHM $> 1000\,\mathrm{km\,s^{-1}}$) emission line for either Hα or Hβ and narrow (FWHM $< 700\,\mathrm{km\,s^{-1}}$) forbidden

[O III] and [N II] emission lines. A. J. Taylor et al. (2024) select sources with broad Hα that have an FWHM $>$ 700 km s^{-1}, the broad component is detected with S/N > 4, and the redshift of the object is determined by at least three strong emission lines.

2.4.2. JADES BL AGN

The sources in JADES are described in detail in R. Maiolino et al. (2024). R. Maiolino et al. (2024) select sources that have a broad component in Hα or Hβ without a broad component in the forbidden [O III]5007 line. Additionally, they require the broad component of the Balmer lines to be at least a factor of 2 broader than the narrow component and have a significance of at least 5σ. The difference in the Bayesian information criterion between a model with only an NL and one with both narrow and broad lines must be greater than 6, i.e., $\mathrm{BIC_{narrow}} - \mathrm{BIC_{broad+narrow}} > 6$.

2.4.3. RUBIES BL AGN

The sources in RUBIES are described in detail in A. J. Taylor et al. (2024). A. J. Taylor et al. (2024) select sources with broad Hα that have an FWHM > 700 km s^{-1}, the broad component is detected with S/N > 4, and the redshift of the object is determined by at least three strong emission lines.

2.5. UV and Optical Slopes

We measure the rest-frame UV and optical slopes for each BL AGN following the procedure described in D. D. Kocevski et al. (2024) and A. J. Taylor et al. (2024). In brief, to compute the UV slope for sources $3.25 < z < 4.75$, we use the F814W, F115W, and F150W filters. For the optical slope, we use the F200W, F277W, and F356W filters. For sources $z > 4.75$, we use the F115W, F150W, and F200W filters for the UV slope and the F277W, F356W, and F444W filters for the optical slope. We fit the UV and optical slopes for each source with a simple power-law fit: $f_\lambda = C\lambda^\beta$, where β is the spectral slope and C is a normalization constant. We find the best-fit power-law function using a Levenberg–Marquardt least-squares method implemented by the `lmfit` package (M. Newville et al. 2016). β_{UV} and β_{opt} values for our BL AGN sample are reported in Table 1.

We visually inspected the galaxy images and find a diversity of morphologies. Most sources have a strong, unresolved component occasionally accompanied by low-surface-brightness extended features and/or clumpy morphologies. A detailed study of morphology is beyond the scope of this work.

3. Emission Line Fitting

We fit the Hα and Hβ Balmer lines in each spectrum with a dual-component, narrow+broad, Gaussian model using the Markov Chain Monte Carlo (MCMC) routine from the Python `emcee` package (D. Foreman-Mackey et al. 2013). The dual-component Gaussian model, adapting the methodology used in R. L. Larson et al. (2023) is

$$f(\lambda)_{\mathrm{dual}} = f_c + f_{\mathrm{nar}} \exp\left(-\frac{1}{2}\frac{(\lambda-\lambda_0)}{\sigma^2_{\mathrm{nar}}}\right) + f_{\mathrm{broad}} \exp\left(-\frac{1}{2}\frac{(\lambda-\lambda_0)}{\sigma^2_{\mathrm{broad}}}\right), \quad (1)$$

where f_c is the continuum flux, which is assumed to be constant; f_{nar} and f_{broad} are the narrow and BL amplitudes; and σ^2_{nar} and $\sigma^2_{\mathrm{broad}}$ are the individual line widths. Both Gaussians share a common line center λ_0.

In the Hα line model, we include additional Gaussian components for the [N II]$\lambda\lambda$6550, 6585 doublet around the Hα line. The intrinsic ratio of the line fluxes of the [N II] lines is fixed to 1:2.94 (D. E. Osterbrock & G. J. Ferland 2006), while their line widths and line centers are constrained to the narrow Hα line.

To fit the Hα emission lines, we run `emcee` using 16 walkers and 25,000 steps and implement a "burn-in" of 10,000 steps, which are discarded from our final chains. We visually inspect the walker chains to confirm that these parameters are sufficient for robust and converged MCMC fits. In our fits, we use flat priors for each model parameter. Additionally, we implement the following constraints on the fitted parameters:

1. $f_{\mathrm{nar}} > 0$ and $f_{\mathrm{broad}} > 0$,
2. $\mathrm{FWHM_{nar}} < 1000$ km s^{-1}, and
3. $\mathrm{FWHM_{broad}} > 1000$ km s^{-1},

and λ_0 is allowed to vary within 250 km s^{-1} of the reported literature redshift values. We confirmed that our best-fit broad and NL widths are statistically consistent with the values reported by Y. Harikane et al. (2023a), R. Maiolino et al. (2024), D. D. Kocevski et al. (2023), and A. J. Taylor et al. (2024).

The above methodology is used to fit Hα, and we discuss our Hβ fitting procedure as follows. For the first run of our Hβ fits, we allow the line width to explore the parameter space indicated above. If the broad component of Hβ is not detected ($f_{\mathrm{broad}} > 3\sigma$), we constrain $\mathrm{FWHM_{broad}}$ to within the measured 1σ bounds of the Hα $\mathrm{FWHM_{broad}}$ and rerun the fit. Even after this iterative fitting process, broad Hβ is significantly detected ($>3\sigma$) in only 4/29 sources. The majority of our sample (25/29) exhibits weak broad Hβ emission despite being selected for significantly broad Hα emission. An example of our best-fit Hα and Hβ emission lines is shown in Figure 2.

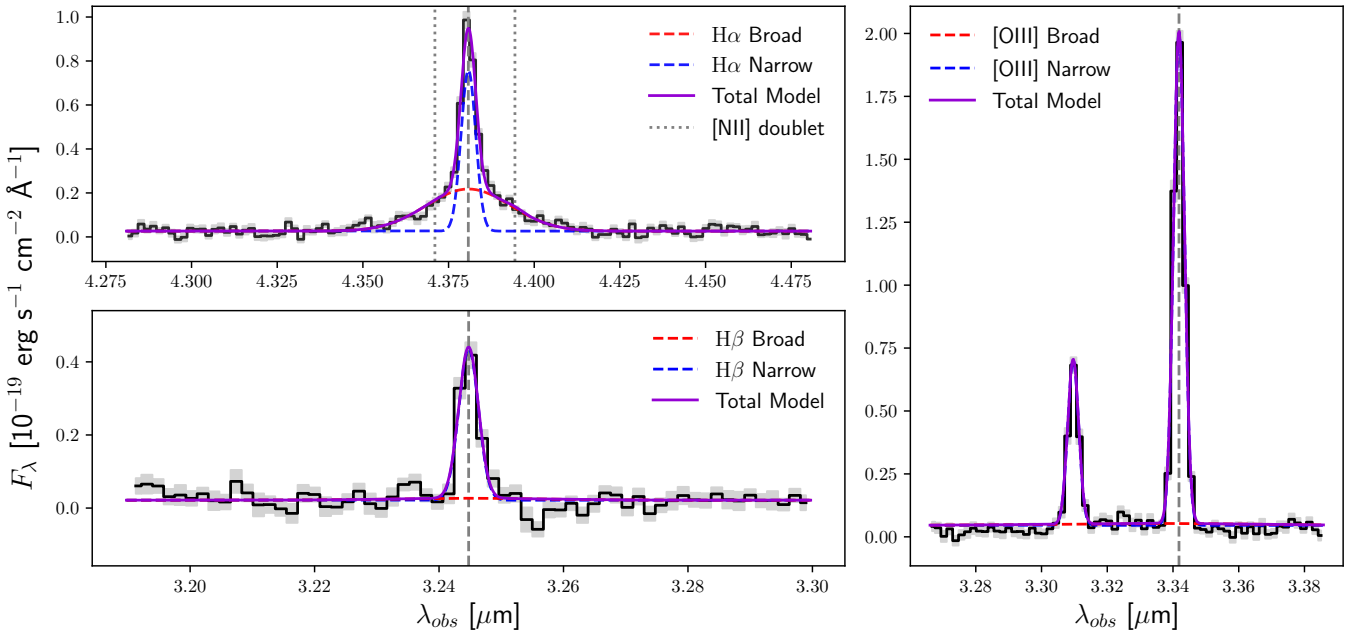

Figure 2. Observed-frame spectra (black histograms) and associated uncertainties (gray error bars) for RUBIES-EGS-47509. The top left panel shows the Hα spectral region, the bottom left panel shows the Hβ spectra region, and the right panel shows the [O III] doublet. Best-fit Gaussians are shown in dark blue for the narrow emission lines and red for the broad components. The total (narrow+broad) best-fit model is shown in purple. Broad Hα is significantly detected in this source (>46σ), but broad Hβ is not. The completed figure set (29 images) includes similar spectra for all BL AGN in our sample.
(The complete figure set (29 images) is available in the online article.)

Additionally, if Hβ $f_{\rm nar}$ is not detected, we constrain FWHM$_{\rm nar}$ to within 1σ of Hα FWHM$_{\rm nar}$. Narrow Hβ is detected in 24/29 sources. We report 3σ upper limits of broad Hβ emission and, when necessary, 3σ upper limits of narrow Hβ emission. Line fluxes for our sample are reported in Table 2.

3.1. Outflows

Large-scale outflows from the interstellar medium (ISM) can be observed as broad emission in the forbidden [O III] lines. To confirm that our sample exhibits broad Hα emission from an AGN and not from an outflow scenario, the [O III] $\lambda\lambda$4959, 5007 doublet is checked for a broad component following the same fitting procedure described in Section 3. The ratio of the [O III] lines is fixed to 2.985:1 (P. J. Storey & C. J. Zeippen 2000).

The vast majority of sources (25/29) with spectral coverage of the [O III] region do not have a significant broad [O III] component. Broad [O III] emission is observed in RUBIES-EGS-50052, also noted in A. J. Taylor et al. (2024). We find a broad Hα component with an FWHM $= 2051^{+31}_{-32}$ km s^{-1} and an [O III] broad component with an FWHM $= 1030^{+17}_{-8}$ km s^{-1}. The [O III] broad component exhibits a significantly different velocity profile than the Hα line, indicative that the origin is a galactic outflow and the system still hosts an AGN. We also detect weak (<4σ) [O III] broad emission in RUBIES-EGS-17416 with an FWHM $= 4943^{+299}_{-435}$ km s^{-1}. Visual inspection of this spectrum indicates that it appears consistent with noise associated with continuum emission.

Spectra for the [O III] doublet region are not available for JADES-GS 8083 and JADES-GN 53757; R. Maiolino et al. (2024) rule out the outflow scenario for these two sources due to the symmetric nature of the broad Hα emission line.

3.2. Stacked Spectra

We produce median-stacked spectra, on both the Hα and Hβ lines, with the sources that show no detection of the broad Hβ component. In total, this is 25/29 of the sources in our sample. We have confirmed with mock spectra, implementing the same narrow+broad Gaussian model as our fitting routine, that the mean BL flux is recovered in the stacked spectrum. Median-stacked spectra let us further explore the differences in the narrow and broad Hα/Hβ ratio for BL AGN by increasing our signal-to-noise ratio. To stack our broad Hβ nondetections, we interpolate our spectra to a common velocity grid of $\sim$60 km s^{-1} per pixel and spanning $\pm$5000 km s^{-1} around the Hα and Hβ lines, which matches the lowest-resolution spectrum in our sample (CEERS-11728, $z = 3.869$). Each spectrum is normalized by the peak of the Hα line flux. We then combine the spectra by taking the median of the fluxes at each velocity pixel position in the velocity grid. Our median-stacked spectra result is shown in Figure 3.

To estimate the errors for our stack, we follow the same stacking procedure as for the flux but median-stack the error spectrum for each source and divide each error pixel by $\sqrt{N}$, where N is the number of sources in the stack. We then compare the normalized absolute median deviation (NMAD) of the continuum region around Hα and Hβ to the median of the flux error over the spectral range around the emission lines. We found in both the Hα and Hβ regions that the errors are slightly overestimated, with NMAD(C_f)/median(σ_f) $= 0.91$ and NMAD(C_f)/median(σ_f) $= 0.60$, respectively. We elected to use the larger median-stacked errors as a conservative approach.

4. Results

The key result of this work is that even after median-stacking the majority of our sources (25/29), broad Hβ emission still remains undetected (<3σ).

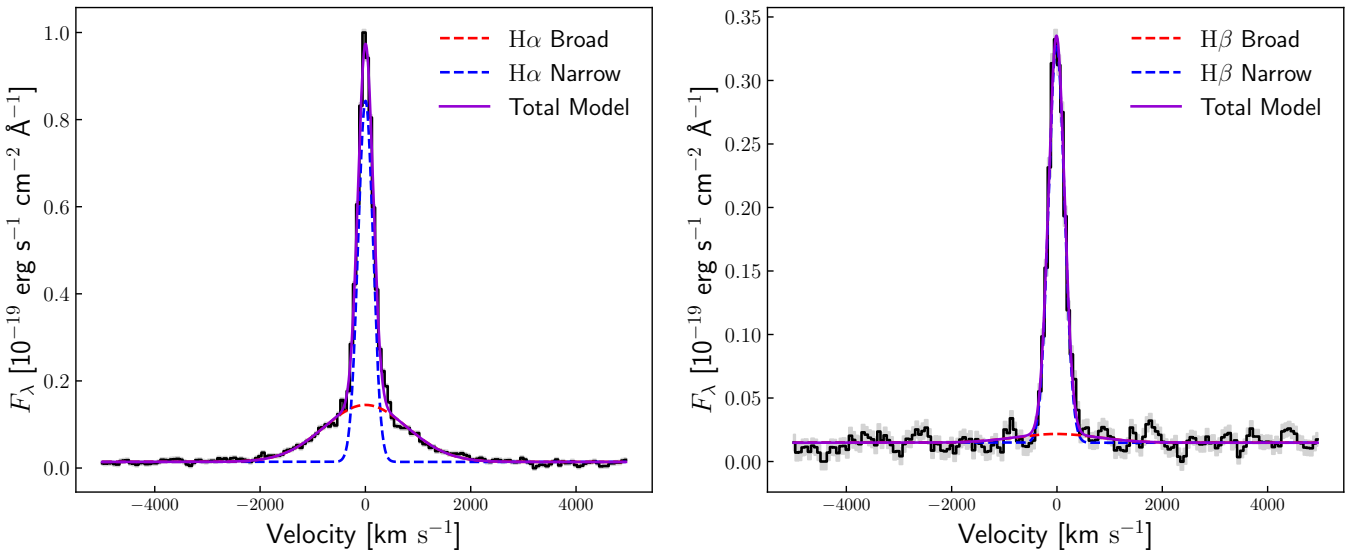

Figure 3. Median-stacked Hα (left) and Hβ (right) emission lines for objects in our sample that exhibit no broad Hβ emission (25/29 sources). Our NL fits are shown in blue, BL fits are shown in red, and the total dual-Gaussian fit is shown in purple. After stacking, broad Hβ emission is still undetected, suggesting that the mean population of AGN show significant dust attenuation in the BLR. The full stacking procedure is described in Section 3.2.

Table 2
AGN Derived Properties

Name	$F_{\mathrm{H}\alpha,\mathrm{narrow}}$ (10^{-19} erg s^{-1} cm^{-2})	$F_{\mathrm{H}\alpha,\mathrm{broad}}$	$\mathrm{FWHM}_{\mathrm{H}\alpha,\mathrm{broad}}$ (km s^{-1})	$F_{\mathrm{H}\beta,\mathrm{narrow}}$ (10^{-19} erg s^{-1} cm^{-2})	$F_{\mathrm{H}\beta,\mathrm{broad}}$	$\mathrm{FWHM}_{\mathrm{H}\beta,\mathrm{broad}}$ (km s^{-1})
CEERS-11728	$96.36^{+2.61}_{-2.52}$	$22.82^{+2.61}_{-2.62}$	1067^{+40}_{-21}	$34.70^{+1.57}_{-1.59}$	<8.12	⋯
JADES-GN-73488	$113.62^{+3.46}_{-3.41}$	$227.91^{+3.85}_{-3.98}$	2098^{+21}_{-22}	$22.33^{+1.22}_{-1.18}$	<7.81	⋯
JADES-GN-11836	$157.16^{+2.40}_{-2.49}$	$39.69^{+3.45}_{-3.44}$	1617^{+62}_{-59}	$44.29^{+1.64}_{-1.65}$	<12.46	⋯
JADES-GN-53757	$41.43^{+3.75}_{-3.65}$	$72.73^{+4.49}_{-4.44}$	1916^{+87}_{-72}	$13.55^{+2.41}_{-2.34}$	<16.23	⋯
CEERS-1665	$453.40^{+6.70}_{-7.21}$	$107.85^{+7.65}_{-7.58}$	1722^{+59}_{-56}	$104.33^{+3.10}_{-3.07}$	<18.55	⋯
CEERS-1236	$12.01^{+1.82}_{-1.19}$	$28.30^{+3.29}_{-3.22}$	3290^{+155}_{-143}	$7.05^{+1.26}_{-1.19}$	<7.72	⋯
JADES-GS-8083	$84.20^{+1.33}_{-1.35}$	$32.54^{+2.00}_{-1.96}$	1728^{+55}_{-52}	$25.86^{+0.98}_{-0.97}$	<4.25	⋯
RUBIES-EGS-46985	$89.19^{+3.55}_{-3.19}$	$61.79^{+3.44}_{-3.40}$	1052^{+34}_{-17}	$26.70^{+2.89}_{-2.83}$	<22.17	⋯
RUBIES-EGS-17416	$24.68^{+1.58}_{-1.49}$	$25.80^{+1.44}_{-1.51}$	1078^{+39}_{-23}	$11.32^{+1.71}_{-1.84}$	<10.29	⋯
JADES-GN-62309	$33.98^{+1.63}_{-1.63}$	$12.05^{+2.39}_{-2.47}$	1076^{+70}_{-40}	$9.63^{+1.35}_{-1.37}$	<12.64	⋯
RUBIES-EGS-17301	$37.98^{+3.68}_{-3.55}$	$54.97^{+9.51}_{-8.57}$	2044^{+253}_{-170}	<3.77	<21.44	⋯
JADES-GN-77652	$27.34^{+3.47}_{-3.01}$	$33.51^{+3.91}_{-4.17}$	1026^{+49}_{-27}	$10.96^{+2.87}_{-2.88}$	<11.22	⋯
RUBIES-EGS-50052	$316.36^{+2.43}_{-2.45}$	$257.55^{+3.22}_{-3.18}$	2052^{+13}_{-14}	$91.02^{+1.75}_{-1.75}$	<38.08	⋯
RUBIES-EGS-13872	$15.61^{+1.11}_{-1.23}$	$11.28^{+1.41}_{-1.44}$	1374^{+128}_{-99}	<4.57	<2.23	⋯
RUBIES-EGS-42046	$635.30^{+12.49}_{-12.81}$	$2026.03^{+20.22}_{-20.20}$	3465^{+17}_{-17}	$30.32^{+4.31}_{-4.25}$	$199.12^{+9.62}_{-9.41}$	2526^{+66}_{-61}
RUBIES-EGS-60935	$77.49^{+4.77}_{-4.67}$	$157.06^{+5.06}_{-5.21}$	2016^{+38}_{-36}	$8.75^{+5.71}_{-3.73}$	$21.55^{+4.23}_{-4.20}$	1149^{+513}_{-116}
RUBIES-EGS-926125	$24.72^{+1.07}_{-1.06}$	$53.48^{+1.62}_{-1.65}$	1586^{+25}_{-25}	$8.35^{+0.85}_{-0.83}$	<9.24	⋯
CEERS-746	$15.34^{+2.70}_{-2.69}$	$48.06^{+2.83}_{-2.89}$	1609^{+75}_{-71}	<0.11	<7.21	⋯
JADES-GN-1093	$25.47^{+1.31}_{-1.31}$	$14.25^{+3.53}_{-3.16}$	2590^{+329}_{-254}	<3.31	<9.71	⋯
RUBIES-UDS-29813	$54.13^{+2.30}_{-2.26}$	$82.79^{+5.25}_{-5.28}$	2809^{+117}_{-111}	<4.34	<6.72	⋯
RUBIES-UDS-19521	$31.84^{+2.46}_{-2.36}$	$28.96^{+4.59}_{-3.69}$	1895^{+380}_{-168}	$10.95^{+1.03}_{-1.03}$	<5.12	⋯
RUBIES-UDS-47509	$39.29^{+1.98}_{-1.94}$	$59.02^{+2.69}_{-2.63}$	1972^{+58}_{-54}	$16.48^{+1.06}_{-1.09}$	<7.87	⋯
RUBIES-EGS-27915	$165.85^{+4.74}_{-4.65}$	$60.93^{+9.82}_{-9.95}$	2795^{+130}_{-118}	$56.57^{+3.50}_{-3.45}$	<47.37	⋯
JADES-GN 61888	$32.23^{+1.99}_{-2.02}$	$33.29^{+2.57}_{-2.58}$	1332^{+58}_{-56}	$8.35^{+0.94}_{-0.98}$	<7.84	⋯
JADES-GS 10013704	$23.00^{+1.05}_{-1.04}$	$40.35^{+2.72}_{-2.74}$	2513^{+75}_{-71}	$7.88^{+0.65}_{-0.64}$	<12.10	⋯
CEERS 00397	$177.50^{+3.03}_{-3.17}$	$33.49^{+4.79}_{-4.76}$	1946^{+117}_{-115}	$64.08^{+1.53}_{-1.54}$	<6.77	⋯
RUBIES-EGS-49140	$207.33^{+22.19}_{-22.72}$	$946.32^{+21.40}_{-23.08}$	2932^{+26}_{-24}	$56.25^{+61.21}_{-16.44}$	$107.72^{+6.26}_{-6.43}$	2254^{+58}_{-53}
JADES-GN 954	$53.28^{+3.92}_{-3.74}$	$159.66^{+8.71}_{-8.22}$	1808^{+51}_{-49}	$14.45^{+1.60}_{-1.58}$	$828.24^{+114.84}_{-115.03}$	2010^{+185}_{-154}
RUBIES-UDS-807469	$10.32^{+2.73}_{-1.98}$	$48.75^{+2.76}_{-2.72}$	1603^{+64}_{-53}	$4.40^{+0.64}_{-0.61}$	<7.27	⋯

Note. We do not report broad Hβ FWHMs for the sources with nondetections; these are denoted with ellipses.

(This table is available in machine-readable form in the online article.)

Table 3
Narrow and Broad Reddening of BL AGN

Name	Narrow Hα/Hβ	Narrow A_v	Broad Hα/Hβ	Broad A_v
CEERS-11728	$2.78^{+0.15}_{-0.14}$	$\simeq$0	>1.83 (>1.83)	$\simeq$0
JADES-GN-73488	$5.09^{+0.32}_{-0.29}$	$1.72^{+0.21}_{-0.21}$	>21.48 (>21.20)	>6.70 (>6.66)
JADES-GN-11836	$3.55^{+0.14}_{-0.14}$	$0.47^{+0.14}_{-0.14}$	>2.14 (>2.10)	$\simeq$0
JADES-GN-53757	$3.06^{+0.71}_{-0.52}$	$\simeq$0	>3.02 (>2.98)	$\simeq$0
CEERS-1665	$4.34^{+0.15}_{-0.14}$	$1.17^{+0.12}_{-0.11}$	>3.84 (>3.58)	$\simeq$0
CEERS-1236	$1.74^{+0.57}_{-0.33}$	$\simeq$0	>2.11 (>2.08)	$\simeq$0
JADES-GS-8083	$3.26^{+0.14}_{-0.13}$	$0.17^{+0.15}_{-0.14}$	>5.11 (>4.92)	>1.73 (>1.60)
RUBIES-EGS-46985	$3.35^{+0.41}_{-0.35}$	$0.26^{+0.40}_{-0.38}$	>1.97 (>1.85)	$\simeq$0
RUBIES-EGS-17416	$2.18^{+0.44}_{-0.30}$	$\simeq$0	>1.76 (>1.69)	$\simeq$0
JADES-GN-62309	$3.53^{+0.61}_{-0.45}$	$0.45^{+0.55}_{-0.48}$	>0.25 (>0.02)	$\simeq$0
RUBIES-EGS-17301	>1.45 (>1.44)	$\simeq$0	>1.49 (>1.49)	$\simeq$0
JADES-GN-77652	$2.50^{+0.96}_{-0.56}$	$\simeq$0	>1.55 (>1.46)	$\simeq$0
RUBIES-EGS-50052	$3.48^{+0.07}_{-0.07}$	$0.40^{+0.07}_{-0.07}$	>6.19 (>6.11)	>2.39 (>2.35)
RUBIES-EGS-13872	>1.38 (>1.36)	$\simeq$0	>2.73 (>2.73)	$\simeq$0
RUBIES-EGS-42046	$20.95^{+3.47}_{-2.65}$	$6.62^{+0.53}_{-0.47}$	$10.18^{+0.51}_{-0.47}$	$4.12^{+0.17}_{-0.16}$
RUBIES-EGS-60935	$8.85^{+6.52}_{-3.47}$	$3.63^{+1.91}_{-1.72}$	$7.29^{+1.77}_{-1.22}$	$2.96^{+0.75}_{-0.63}$
RUBIES-EGS-926125	$2.96^{+0.35}_{-0.30}$	$\simeq$0	>4.67 (>4.62)	>1.42 (>1.38)
CEERS-746	>1.85 (>1.80)	$\simeq$0	>4.99 (>4.95)	>1.65 (>1.62)
JADES-GN 1093	>2.30 (>2.27)	$\simeq$0	>0.44 (>0.36)	$\simeq$0
RUBIES-UDS-29813	>3.91 (>2.98)	>0.81 (>0.80)	>7.36 (>6.73)	$\simeq$0
RUBIES-UDS-19521	$2.91^{+0.37}_{-0.33}$	$\simeq$0	>3.55 (>3.51)	$\simeq$0
RUBIES-UDS-47509	$2.38^{+0.20}_{-0.19}$	$\simeq$0	>5.15 (>5.13)	>1.76 (>1.74)
RUBIES-EGS-27915	$2.93^{+0.21}_{-0.19}$	$\simeq$0	>0.69 (>0.63)	$\simeq$0
JADES-GN-61888	$3.86^{+0.57}_{-0.45}$	$0.75^{+0.48}_{-0.43}$	>3.11 (>3.09)	>0.01 (0)
JADES-GS-10013704	$2.92^{+0.28}_{-0.25}$	$\simeq$0	>2.63 (>2.60)	$\simeq$0
CEERS-397	$2.77^{+0.84}_{-0.08}$	$\simeq$0	>2.84 (>2.82)	$\simeq$0
RUBIES-EGS-49140	$2.73^{+1.28}_{-1.59}$	$\simeq$0	$8.97^{+0.593}_{-0.526}$	$3.68^{+0.222}_{-0.209}$
JADES-GN-954	$3.69^{+0.52}_{-0.43}$	$0.60^{+0.46}_{-0.43}$	$5.49^{+1.37}_{-1.03}$	$1.98^{+0.77}_{-0.72}$
RUBIES-UDS-807469	$2.37^{+0.72}_{-0.54}$	$\simeq$0	>5.19 (>5.13)	>1.79 (>1.75)

Note. Here we are reporting the 3σ lower limit on the Balmer decrement measurements when necessary. The 5σ limit is additionally given in the parentheses.
(This table is available in machine-readable form in the online article.)

The narrow and broad Hα and Hβ emission line fluxes and corresponding FWHM$_{broad}$ for the individual sources in our sample are reported in Table 2, and the upper limits on Hβ are reported when necessary. The vast majority of our sources (25/29) do not have detected broad Hβ line emission despite having significantly (>5σ) detected broad Hα emission. Additionally, 5 of the 29 sources have no (<3σ) detected Hβ emission at all (broad or narrow).

To estimate dust attenuation from the measured Balmer decrement, we follow the prescription provided by I. G. Momcheva et al. (2013). We assume a D. Calzetti (1997) attenuation curve and an intrinsic Balmer line ratio of $(\mathrm{H}\alpha/\mathrm{H}\beta)_{\mathrm{int}} = 3.1$, the latter of which is appropriate for AGN broad line region (BLR) and narrow line region (NLR) gas conditions (D. E. Osterbrock & G. J. Ferland 2006). When broad Hβ or narrow+broad Hβ is undetected, we determine the 3σ and 5σ lower limit on the Hα/Hβ ratio. The full list of narrow and broad Balmer decrements (including both detections and limits) is found in Table 3. Emission lines associated with star-forming regions instead have an intrinsic line ratio of $(\mathrm{H}\alpha/\mathrm{H}\beta)_{\mathrm{int}} = 2.86$ (for $n_e = 10^2\,\mathrm{cm}^{-3}$, $T_e = 10^4\,\mathrm{K}$, case B recombination), which would lead to slightly larger dust attenuation estimates than our assumption of $(\mathrm{H}\alpha/\mathrm{H}\beta)_{\mathrm{int}} = 3.1$ for AGN-ionized gas. This choice in intrinsic ratio does not affect the general conclusions of this study.

Figure 4 shows the measured Balmer decrements and inferred V-band dust attenuation for the 29 AGN in our sample. The majority (26/29) of our sources have NL Hα/Hβ ratios that are consistent with the intrinsic value and have little to no attenuation. The lower limits in broad Hβ are consistent with a wide range of BL attenuation; these sources are shown as open symbols in Figure 4. Additionally, we investigated the broad Hα flux fraction ($F_{\mathrm{H}\alpha,\mathrm{broad}}/F_{\mathrm{H}\alpha,\mathrm{total}}$) with the broad Balmer decrement but are unable to provide any constraints on this relationship due to the majority of our (25/29) sources exhibiting no broad Hβ emission.

Three sources, JADES-GN-73488, RUBIES-EGS-42046, and RUBIES-EGS-60935, show significant NL and BL attenuation. Our most extremely attenuated source has a BL $A_v > 6.70$. This suggests an intrinsically high emission line strength, and we interpret the dustiest sources as unusual systems that are not representative of the bulk of the $z > 3.5$ BL AGN sample (K. Davis et al. 2024). Specific NL and BL Balmer ratios are given in Table 3.

JADES-GN-954 exhibits both broad Hα and Hβ emission and has greater dust attenuation in the BL region. Additionally, RUBIES-EGS-60935 has detected, but not strong (>2σ) broad Hβ emission and shows similar attenuation in the narrow and broad regions. Nine individual sources show broad Hα/Hβ > narrow Hα/Hβ; M. Killi et al. (2024) also find much higher attenuation in the BLR for a single source ($z \sim 4.53$).

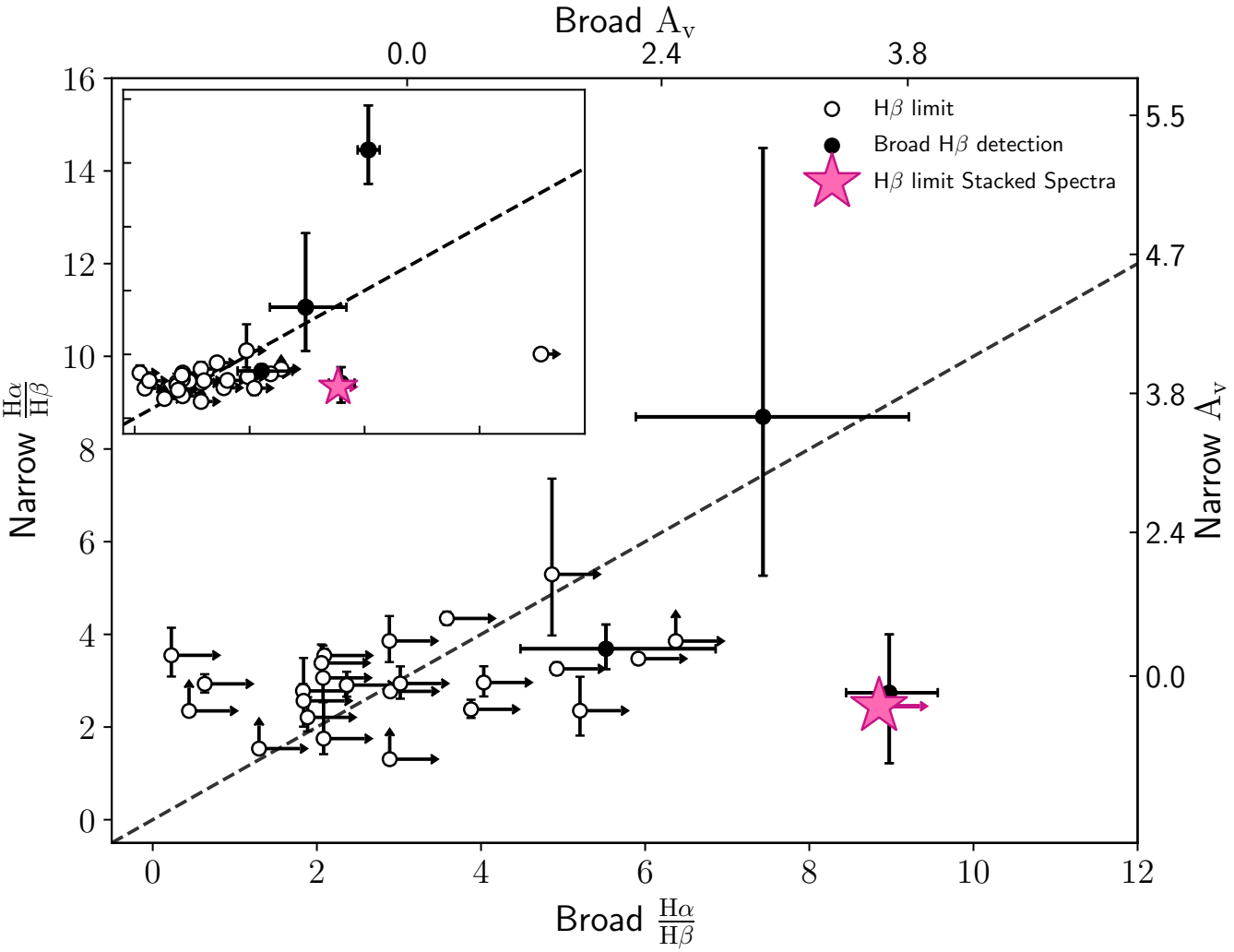

Figure 4. Narrow Hα/Hβ vs. broad Hα/Hβ for the sample of 29 BL AGN. Filled circles represent sources with detected broad Hβ emission, while the open circles are galaxies with undetected broad Hβ and are plotted using the 3σ upper limit of broad Hβ. The pink star represents the stack of sources with no detected broad Hβ and is plotted using the 3σ upper limit of broad Hβ. The one-to-one line is shown by the dashed black line. An inset is included in the top left to show two extremely reddened sources, RUBIES-EGS-42406 (black circle) with detected broad Hβ emission and JADES 73488 (open circle). The A_v for the broad and narrow flux ratios, calculated with the D. Calzetti (1997) dust law and described in Section 4, are shown on the dual *x*- and *y*-axes, respectively. Twelve out of 29 sources fall firmly below the one-to-one line, indicative of broad Hα/Hβ > narrow Hα/Hβ.

Sources in our sample with Hα/Hβ < narrow Hα/Hβ falling left of the one-to-one line in Figure 4 generally have lower signal-to-noise ratios than sources to the right of the line. We expect deeper observations of these objects to show the result shown by the stacked, broad Hα/Hβ > narrow Hα/Hβ.

In addition to the individual sources, we measure the narrow and broad Balmer decrements for our stacked spectra. We find narrow $H\alpha/H\beta = 2.47^{+0.05}_{-0.05}$ and broad Hα/Hβ > 8.85. The NL measurement is consistent with no attenuation, and the BL ratio implies $A_v > 3.63$ for a D. Calzetti (1997) attenuation curve. The median-stacked spectra is shown as a pink star in Figure 4. For an SMC attenuation curve (M. L. Prevot et al. 1984; P. Bouchet et al. 1985), we find a BL $A_v > 2.67$.

5. Discussion and Conclusions

In this work, we present dust attenuation measurements for 29 BL identified AGN in the JWST deep fields. We also further investigate the optical dust attenuation of these sources using a stacking analysis of sources that have no significantly detected broad Hβ emission. The nondetection of Hβ and significantly detected Hα (>15σ) after stacking indicates that these sources are, on average, heavily dust attenuated in the rest-frame optical. Narrow $H\alpha/H\beta = 2.55^{+0.07}_{-0.07}$ (consistent with zero dust attenuation)[19] and broad Hα/Hβ > 8.85 ($A_V > 3.63$) for the stack suggest that the origin of the narrow and broad components of the emission lines originate from different regions in the galaxy. The broad emission lines are emitted from near the AGN, and their high attenuation implies that the red optical colors of LRDs are driven by dust-attenuated emission from the central AGN. Meanwhile, the narrow lines are presumably emitted from extended scales, and the low attenuation of the narrow lines implies that the blue/UV colors of LRDs are dominated by star formation processes in the host galaxy. The narrow emission lines are still associated with the AGN but originate on extended galactic

[19] The stacked, narrow Hα/Hβ is significantly lower than the fiducial value of Hα/Hβ = 2.86. This likely implies higher electron temperature for the gas (for example, $T_e = 2 \times 10^4$ K results in Hα/Hβ = 2.75 for the case B recombination), consistent with previous work studying the ISM conditions of high-redshift galaxies (e.g., J. R. Trump et al. 2023; B. E. Backhaus et al. 2024; R. L. Sanders et al. 2024).

scales (C. M. Urry & P. Padovani 1995); NLR sizes are found to be on the order of 3–10 kpc (N. Bennert et al. 2002; J. E. Greene et al. 2011; K. N. Hainline et al. 2014).

The narrow Balmer lines in the majority of our sources (26/29) are consistent with little to no dust attenuation. Our distribution of NL Balmer decrements is consistent with A. E. Shapley et al. (2023) measurements for a population of non-BL AGN. L. Sandles et al. (2024) also find consistently low Balmer decrements, where the median is 2.88 ± 0.08 for a sample of 51 galaxies. The NL Balmer decrement of the stacked spectra also shows no dust attenuation. The central AGN in these sources are consistently much more reddened than what is seen on the galactic scale, further suggesting that the blue UV colors seen in the SEDs is from star formation in the galaxy.

We additionally tested for correlations between both the narrow and broad Balmer decrements and the UV and optical slopes of each source. We find no significant trends in any of these relationships. We note that the lack of a correlation between the narrow $H\alpha/H\beta$ and the β_{opt} slope is consistent with our picture in which the (generally unreddened) narrow emission lines are associated with the galaxy and the (generally reddened) optical continuum is associated with the AGN. The lack of an observed correlation between the broad $H\alpha/H\beta$ and β_{opt} slope is likely due to widespread lower limits in our measured BL Balmer decrements.

The source of attenuation around the central AGN could be explained by a dusty torus of obscuring gas near the AGN (J. H. Krolik & M. C. Begelman 1988). However, mid-infrared observations of LRDs from photometric data are inconsistent with the dusty torus model (P. G. Pérez-González et al. 2024; C. C. Williams et al. 2024).[20] Rather than a canonical torus, the AGN may be attenuated by larger-scale dust in the galaxy nucleus that is somewhat cooler than a torus but is still much more compact than the host galaxy starlight (J. Buchner & F. E. Bauer 2017). The observed dust attenuation may also be described by a polar dust model (G. Yang et al. 2020; V. Buat et al. 2021) that is more compact than the NL region but colder than the torus.

Higher attenuation around the AGN is also consistent with the lack of X-ray detections for these sources (R. Maiolino et al. 2025). Two of our sources, RUBIES-EGS-42046 and RUBIES-EGS-49140, show strong Balmer absorption lines, which require extremely high densities of neutral hydrogen gas (P. B. Hall 2007; K. Inayoshi & R. Maiolino 2025; J. Matthee et al. 2024). High-density absorbing material around the AGN may dampen X-ray emission and explain the nondetections of the LRDs in deep X-ray fields, even after a stacking analysis. Additionally, our results show a dramatic bimodality of the BL and NL attenuation for high-redshift AGN, which suggests that these regions in the galaxy are physically distinct (M. Volonteri et al. 2025). The dramatically different attenuations of the broad and narrow lines disfavors non-AGN models (J. F. W. Baggen et al. 2024; M. Kokubo & Y. Harikane 2024) due to gas that is more likely to have continuous velocity and attenuation distributions.

The large population of BL AGN and LRDs at high redshifts is one of the biggest surprises revealed by JWST. This work shows, on average, high-redshift BL AGN have highly attenuated nuclei but little to no attenuation affecting the extended host galaxy. However, currently available JWST spectroscopy is insufficient to resolve the nature of the dust in individual sources and to study the distribution of dust attenuation as a function of galaxy and AGN properties. This population represents a look into obscured BH formation growth in early epochs and is important to fully understanding the BH–galaxy coevolution. Deeper and/or NIRSpec integral field unit spectroscopy is needed to further disentangle the obscured nature of AGN and host galaxy emission and growth at cosmic dawn.

[20] We note that there is no overlap between the sources studied in C. C. Williams et al. (2024) and P. G. Pérez-González et al. (2024) with our sample. Both of these studies analyzed sources in the GOODS-S field; our sample contains only two sources in this field.

Acknowledgments

We thank the JADES, RUBIES, and PRIMER teams for their effort in designing and executing their programs and for making the data publicly available. We acknowledge the work of our colleagues in the CEERS collaboration and everyone involved in the JWST mission. M.B., J.R.T., and K.D. acknowledge support from NASA grants JWST-ERS-01345, JWST-AR-01721, and NSF grant CAREER-1945546.

Facility: JWST.

Software: astropy: Astropy Collaboration et al. (2013, 2018, 2022), scipy: P. Virtanen et al. (2020), emcee: (D. Foreman-Mackey et al. 2013), numpy: C. R. Harris et al. (2020)

ORCID iDs

Madisyn Brooks https://orcid.org/0000-0001-5384-3616
Raymond C. Simons https://orcid.org/0000-0002-6386-7299
Jonathan R. Trump https://orcid.org/0000-0002-1410-0470
Anthony J. Taylor https://orcid.org/0000-0003-1282-7454
Micaela B. Bagley https://orcid.org/0000-0002-9921-9218
Bren Backhaus https://orcid.org/0000-0001-8534-7502
Kelcey Davis https://orcid.org/0000-0001-8047-8351
Véronique Buat https://orcid.org/0000-0003-3441-903X
Nikko J. Cleri https://orcid.org/0000-0001-7151-009X
Alexander de la Vega https://orcid.org/0000-0002-6219-5558
Steven L. Finkelstein https://orcid.org/0000-0001-8519-1130
Michaela Hirschmann https://orcid.org/0000-0002-3301-3321
Benne W. Holwerda https://orcid.org/0000-0002-4884-6756
Dale D. Kocevski https://orcid.org/0000-0002-8360-3880
Anton M. Koekemoer https://orcid.org/0000-0002-6610-2048
Ray A. Lucas https://orcid.org/0000-0003-1581-7825
Fabio Pacucci https://orcid.org/0000-0001-9879-7780
Lise-Marie Seillé https://orcid.org/0000-0001-7755-4755

References

Akins, H. B., Casey, C. M., Lambrides, E., et al. 2024, arXiv:2406.10341
Ananna, T. T., Bogdán, Á., Kovács, O. E., Natarajan, P., & Hickox, R. C. 2024, ApJL, 969, L18
Arrabal Haro, P., Dickinson, M., Finkelstein, S. L., et al. 2023, ApJL, 951, L22
Astropy Collaboration, Price-Whelan, A. M., Lim, P. L., et al. 2022, ApJ, 935, 167
Astropy Collaboration, Price-Whelan, A. M., Sipőcz, B. M., et al. 2018, AJ, 156, 123

Astropy Collaboration, Robitaille, T. P., Tollerud, E. J., et al. 2013, A&A, 558, A33
Backhaus, B. E., Trump, J. R., Pirzkal, N., et al. 2024, ApJ, 962, 195
Baggen, J. F. W., van Dokkum, P., Brammer, G., et al. 2024, ApJL, 977, L13
Barro, G., Pérez-González, P. G., Kocevski, D. D., et al. 2024, ApJ, 963, 128
Bennert, N., Falcke, H., Schulz, H., Wilson, A. S., & Wills, B. J. 2002, ApJL, 574, L105
Bouchet, P., Lequeux, J., Maurice, E., Prevot, L., & Prevot-Burnichon, M. L. 1985, A&A, 149, 330
Bromm, V., & Loeb, A. 2003, ApJ, 596, 34
Buat, V., Mountrichas, G., Yang, G., et al. 2021, A&A, 654, A93
Buchner, J., & Bauer, F. E. 2017, MNRAS, 465, 4348
Bunker, A. J., Cameron, A. J., Curtis-Lake, E., et al. 2024, A&A, 690, A288
Calzetti, D. 1997, AJ, 113, 162
Davis, K., Trump, J. R., Simons, R. C., et al. 2024, ApJ, 974, 42
de Graaff, A., Brammer, G., Weibel, A., et al. 2025, A&A, 697, A189
D'Eugenio, F., Cameron, A. J., Scholtz, J., et al. 2025, ApJS, 277, 4
Durodola, E., Pacucci, F., & Hickox, R. C. 2025, ApJ, 985, 169
Eisenstein, D. J., Willott, C., Alberts, S., et al. 2023, arXiv:2306.02465
Ferruit, P., Jakobsen, P., Giardino, G., et al. 2022, A&A, 661, A81
Finkelstein, S., Bagley, M., & Yang, G. 2023, Data from The Cosmic Evolution Early Release Science Survey (CEERS), STScI/MAST, doi:10.17909/Z7P0-8481
Finkelstein, S. L., Bagley, M. B., Ferguson, H. C., et al. 2023, ApJL, 946, L13
Foreman-Mackey, D., Hogg, D. W., Lang, D., & Goodman, J. 2013, PASP, 125, 306
Greene, J. E., Labbe, I., Goulding, A. D., et al. 2024, ApJ, 964, 39
Greene, J. E., Zakamska, N. L., Ho, L. C., & Barth, A. J. 2011, ApJ, 732, 9
Hainline, K. N., Hickox, R. C., Greene, J. E., et al. 2014, ApJ, 787, 65
Hall, P. B. 2007, AJ, 133, 1271
Harikane, Y., Ouchi, M., Oguri, M., et al. 2023b, ApJS, 265, 5
Harikane, Y., Zhang, Y., Nakajima, K., et al. 2023a, ApJ, 959, 39
Harris, C. R., Millman, K. J., van der Walt, S. J., et al. 2020, Natur, 585, 357
Inayoshi, K., & Maiolino, R. 2025, ApJL, 980, L27
Inayoshi, K., Visbal, E., & Haiman, Z. 2020, ARA&A, 58, 27
Juodžbalis, I., Ji, X., Maiolino, R., et al. 2024, MNRAS, 535, 853
Kelly, B. C., & Shen, Y. 2013, ApJ, 764, 45
Killi, M., Watson, D., Brammer, G., et al. 2024, A&A, 691, A52
Kocevski, D. D., Finkelstein, S. L., Barro, G., et al. 2024, arXiv:2404.03576
Kocevski, D. D., Onoue, M., Inayoshi, K., et al. 2023, ApJL, 954, L4
Kokorev, V., Fujimoto, S., Labbe, I., et al. 2023, ApJL, 957, L7
Kokubo, M., & Harikane, Y. 2024, arXiv:2407.04777
Krolik, J. H., & Begelman, M. C. 1988, ApJ, 329, 702
Labbe, I., Greene, J. E., Bezanson, R., et al. 2025, ApJ, 978, 92
Lambrides, E., Garofali, K., Larson, R., et al. 2024, arXiv:2409.13047
Larson, R. L., Finkelstein, S. L., Kocevski, D. D., et al. 2023, ApJL, 953, L29
Li, Z., Inayoshi, K., Chen, K., Ichikawa, K., & Ho, L. C. 2025, ApJ, 980, 36
Lodato, G., & Natarajan, P. 2006, MNRAS, 371, 1813
Lyu, J., Alberts, S., Rieke, G. H., et al. 2024, ApJ, 966, 229
Maiolino, R., Risaliti, G., Signorini, M., et al. 2025, MNRAS, 538, 1921
Maiolino, R., Scholtz, J., Curtis-Lake, E., et al. 2024, A&A, 691, A145
Matsuoka, Y., Strauss, M. A., Kashikawa, N., et al. 2018, ApJ, 869, 150
Matthee, J., Naidu, R. P., Brammer, G., et al. 2024, ApJ, 963, 129
Momcheva, I. G., Lee, J. C., Ly, C., et al. 2013, AJ, 145, 47
Newville, M., Stensitzki, T., Allen, D. B., et al., 2016 Lmfit: Non-Linear Least-Square Minimization and Curve-Fitting for Python Astrophysics Source Code Library, ascl: 1606.014
Osterbrock, D. E., & Ferland, G. J. 2006, Astrophysics of Gaseous Nebulae and Active Galactic Nuclei (Sausalito, CA: Univ. Science Books),
Pacucci, F., & Narayan, R. 2024, ApJ, 976, 96
Pacucci, F., Nguyen, B., Carniani, S., Maiolino, R., & Fan, X. 2023, ApJL, 957, L3
Pérez-González, P. G., Barro, G., Rieke, G. H., et al. 2024, ApJ, 968, 4
Planck Collaboration, Aghanim, N., Akrami, Y., et al. 2020, A&A, 641, A6
Prevot, M. L., Lequeux, J., Maurice, E., Prevot, L., & Rocca-Volmerange, B. 1984, A&A, 132, 389
Rieke, M., Robertson, B., Tacchella, S., et al. 2023, Data from the JWST Advanced Deep Extragalactic Survey (JADES), STScI/MAST, doi:10.17909/8TDJ-8N28
Sanders, R. L., Shapley, A. E., Topping, M. W., Reddy, N. A., & Brammer, G. B. 2024, ApJ, 962, 24
Sandles, L., D'Eugenio, F., Maiolino, R., et al. 2024, A&A, 691, A305
Shapley, A. E., Sanders, R. L., Reddy, N. A., Topping, M. W., & Brammer, G. B. 2023, ApJ, 954, 157
Storey, P. J., & Zeippen, C. J. 2000, MNRAS, 312, 813
Taylor, A. J., Finkelstein, S. L., Kocevski, D. D., et al. 2024, arXiv:2409.06772
Trump, J. R., Arrabal Haro, P., Simons, R. C., et al. 2023, ApJ, 945, 35
Übler, H., Maiolino, R., Curtis-Lake, E., et al. 2023, A&A, 677, A145
Urry, C. M., & Padovani, P. 1995, PASP, 107, 803
Vestergaard, M., & Osmer, P. S. 2009, ApJ, 699, 800
Virtanen, P., Gommers, R., Oliphant, T. E., et al. 2020, NatMe, 17, 261
Volonteri, M., Haardt, F., & Madau, P. 2003, ApJ, 582, 559
Volonteri, M., Trebitsch, M., Greene, J. E., et al. 2025, A&A, 695, A33
Wang, B., de Graaff, A., Davies, R. L., et al. 2025, ApJ, 984, 121
Williams, C. C., Alberts, S., Ji, Z., et al. 2024, ApJ, 968, 34
Yang, G., Boquien, M., Buat, V., et al. 2020, MNRAS, 491, 740
Yue, M., Eilers, A.-C., Ananna, T. T., et al. 2024, ApJL, 974, L26